www.nature.com/scientificreports

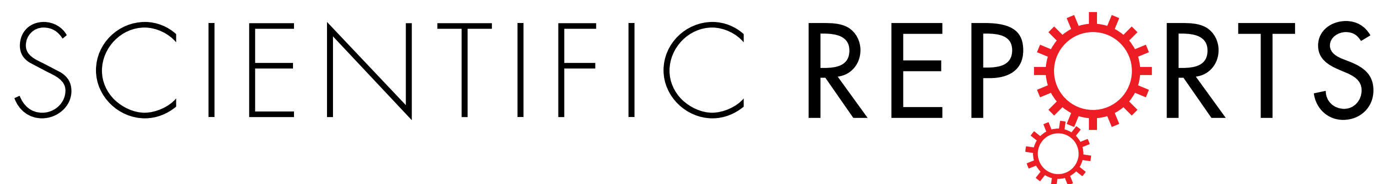

OPEN

Growth Mechanisms and Electronic Properties of Vertically Aligned MoS_2

Received: 27 February 2018
Accepted: 1 October 2018
Published online: 07 November 2018

Chen Stern[1], Shmuel Grinvald[1], Moshe Kirshner[1], Ofer Sinai[1], Mark Oksman[1], Hadas Alon[1,2], Oren E. Meiron[3], Maya Bar-Sadan[3], Lothar Houben[4] & Doron Naveh[1]

Thin films of layered semiconductors emerge as highly promising materials for energy harvesting and storage, optoelectronics and catalysis. Their natural propensity to grow as oriented crystals and films is one of their distinct properties under recent focal interest. Specifically, the reaction of transition metal films with chalcogen vapor can result in films of vertically aligned (VA) layers, while metal-oxides react with chalcogens in vapor phase to produce horizontally aligned crystals and films. The growth mechanisms of vertically oriented films are not yet fully understood, as well as their dependence on the initial metal film thickness and growth conditions. Moreover, the resulting electronic properties and the role of defects and disorder had not yet been studied, despite their critical influence on catalytic and device performance. In this work, we study the details of oriented growth of MoS_2 with complementary theoretical and experimental approaches. We present a general theoretical model of diffusion-reaction growth that can be applied to a large variety of layered materials synthesized by solid-vapor reaction. Moreover, we inspect the relation of electronic properties to the structure of vertically aligned MoS_2 and shed light on the density and character of defects in this material. Our measurements on Si-MoS_2 p-n hetero-junction devices point to the existence of polarizable defects that impact applications of vertical transition-metal dichalcogenide materials.

The growing interest in layered inorganic materials over the last decade was stimulated by the development of novel synthetic methods. Among such methods chemical vapor deposition (CVD) dominated the production methods of scalable, device-grade transition-metal dichalcogenides (TMDC)[1–3]. In turn, the success of the synthetic research has propelled the research on novel device applications[4–7] and fundamental physics of layered materials[8–10]. Hitherto, CVD growth of TMDCs was mostly focused on the growth of ultrathin, few-layer crystals and heterostructures[11–15]. The recent reemergence of vertically aligned (VA) thin films of TMDCs is imperative to diverse device applications and of fundamental interest, owing to their unique growth mechanism[16–19]. Moreover, thin VA-MoS_2 films were established as scalable, high quality electronic materials, enabling highly-responsive near infrared photodetectors[20–24] and energy storage devices based on Li^+ and Na^+ intercalation[25,26]. However, the role of defects and crystalline disorder can be critically important in these materials. Solar energy harvesting with self-driven photodiodes[27] of VA-MoS_2 on P-Si yields relatively low quantum efficiency due to the enhanced recombination rates associated with defects in VA-MoS_2. Catalytic activity of VA-MoS_2 is associated with its high density of edge states and is also prone to be influenced by defects and crystalline disorder[17]. Therefore, understanding the formation and properties of defects and disorder in VA-MoS_2 is critically important for a variety of applications and may pave the way for achieving the full potential of vertically aligned layered compounds.

Early studies of VA-MoS_2 deposition were conducted by RF magnetron sputtering[28,29]. More recently, studies on the CVD growth mechanisms of VA-MoS_2 found that sulfurization of thin Mo films changes character from planar to vertical crystal growth, controlled by the thickness of the Mo film[30,31]. Specifically, a critical thickness of 5 nm was found to be the threshold for vertical growth, while sulfurization of thinner metal films resulted in planar oriented MoS_2[19]. The vertical orientation of VA-TMDCs is attributed to a diffusion-driven growth mechanism[19,32,33]. In this mechanism, sulfur diffuses through the Van der Waals interlayer gap at a much higher rate

[1]Faculty of Engineering and Institute for Nanotechnology and Advanced Materials, Bar-Ilan University, Ramat Gan, Israel. [2]Department of Chemistry and Institute for Nanotechnology and Advanced Materials, Bar-Ilan University, Ramat Gan, Israel. [3]Department of Chemistry, Ben Gurion University, Beer-Sheva, Israel. [4]Department of Chemical Research Support, Weizmann Institute of Science, Rehovot, Israel. Correspondence and requests for materials should be addressed to D.N. (email: doron.naveh@biu.ac.il)

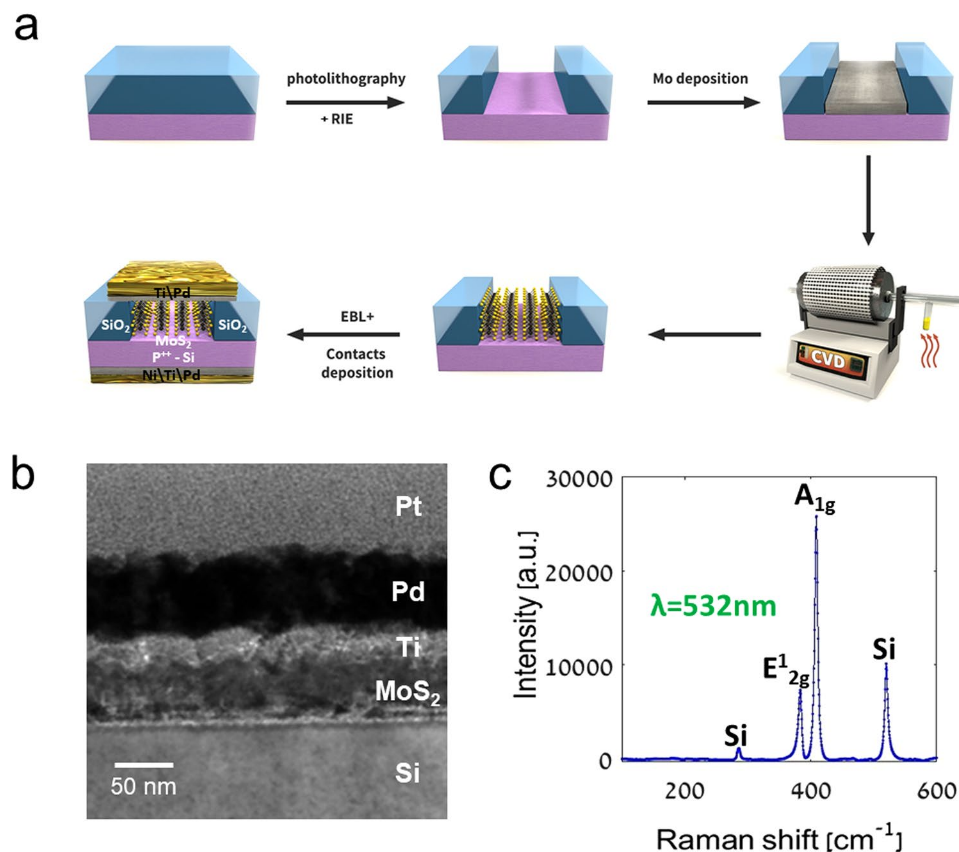

Figure 1. (**a**) Graphical representation of a MoS_2 device fabrication process: 90 nm SiO_2/Si selective etch by photolithography and reactive-ion etching, Mo deposition and lift-off, sulfurization growth of VA-MoS_2, and metallization of devices. (**b**) A cross-sectional TEM micrograph of the resulting device. (**c**) Raman spectrum of the MoS_2 taken immediately after growth.

than across the crystal layers – and thus the preferred orientation of the growth is established from kinetic considerations. However, the details of the vertical alignment mechanism and the turning point from planar to vertical growth are not yet fully understood. These details are significant for the advancement of several important device applications across multiple fields[32,34–37]. Moreover, the impact of a multi-domain (vertical and randomly oriented) structure on the electronic properties of MoS_2 remains unclear. In this work, we study the formation mechanism of VA-MoS_2 films on P-Si and their charge carrier characteristics as resolved from transport measurements of p-n junction devices.

Results and Discussion

Our devices are constructed from 70 nm thick MoS_2 grown on P^+-Si by CVD in the following process: 90 nm Si/SiO_2 wafers were patterned by photolithography and etched to form through-oxide vias (Fig. 1a), on which 30 nm metal Mo was deposited and lifted-off. Mo films were then sulfurized under flow of 30 sccm nitrogen in background pressure of 5 mTorr, carrying sulfur vapor from a boat heated to 150 °C. The sample was kept at 800 °C during the growth. Clean Raman spectra were taken from the samples at a parallel geometry between the laser line and the c-axis of the crystal, with linearly polarized light (Fig. 1c), obtaining the signal of 2H-MoS_2 and crystalline Si, without traces of molybdenum silicide. Then, a second lithographic process was applied for metallizing the grown MoS_2 with Ti/Pd contacts (Fig. 1b).

A detailed characterization of the MoS_2 layer was performed with cross-section transmission electron microscopy of samples as shown in Fig. 2, with two types of thermal processing; in both cases a thin film of Mo on Si/SiO_2 (as in Fig. 1) were sulfurized at 800 °C for two hours under continuous temperature ramping. Interestingly, samples of fast temperature ramping (20 °C/min) exhibit thicker domains of randomly oriented crystals as compared to slow temperature ramping samples (5 °C/min). Details of the process are given below and in the supporting information. Temperature cycles are displayed for clarity in Fig. S1. The proposed growth mechanism assumes that during the reaction, the growth front propagates into the Mo film from the vapor-solid interface inwards, finally reaching the Si substrate. Complementary, the case of thick Mo films representing the growth process at the semi-infinite samples was studied on thick Mo foils to elucidate the limit of long reaction time and depth (Figs S2 and S3), as discussed in the supplementary information. During the reaction on Mo on Si/SiO_2, the growth front propagates into the Mo film, from the vapor-solid interface inwards, finally reaching the Si substrate. The image for the fast growth (Fig. 2a) reveals a gradual establishment of preferred crystallographic orientation. The MoS_2 is crystalline along the reaction path, initially showing random orientation that after a threshold thickness becomes a vertically oriented layer.

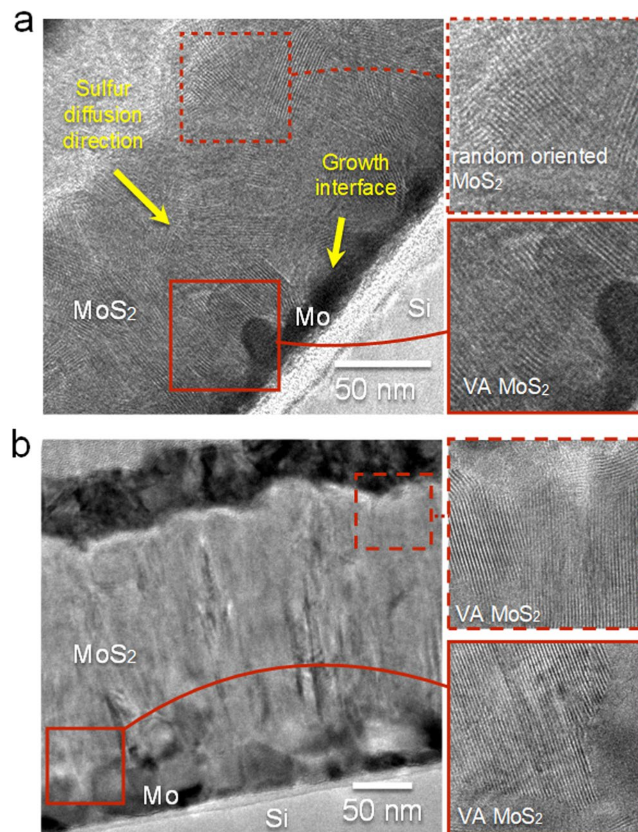

Figure 2. TEM micrograph of VA-MoS_2 grown on Si substrate at 800 °C for 2 h with a temperature ramping rate of 20 °C/min (**a**) and 5 °C/min (**b**), respectively. Insets show the magnified view of vertically aligned MoS_2 in the initial growth at the top (dashed rectangle) and at the growth interface (solid rectangle). The surface reaction results in an initial growth of a significantly thick randomly oriented MoS_2 layer for fast growth, in contrast with slow growth where the layers are vertically aligned (dashed rectangle).

Thus, the crystal orientation ordering towards VA-MoS_2 started only after an incubation thickness that we term as "surface reaction". Following the surface reaction a strongly preferred orientation is evidenced by the sharpening of the orientation distribution around the perpendicular axis (Figs S4 and S5), in proximity to the substrate. In order to understand this growth process and the parameters controlling the thickness of the disordered layer formed at the early stages of the reaction, we quantified the crystal orientation of the films as a function of the reaction coordinate (Fig. S4). Results of the quantification procedure are displayed in Fig. S5. This transition in growth leaves a 30–40 nm thick randomly oriented layer at the fast growth conditions. In contrast, for the sample grown at slow growth conditions (Fig. 2b), the typical thickness of the surface reaction layer is much smaller than that of the fast growth (<10 nm), in agreement with previous studies[16,19,33]. Under low growth rate the disordered layer is thinner, thus indicating a lower surface reactivity and dominant diffusion-limited growth mechanism. The examples of Fig. 2 shows that the thickness of the randomly oriented film is strongly affected by the growth kinetics, yet the growth mechanisms and the role of the disordered layer were not thoroughly examined.

Here, we present a model describing the growth process resulting in the co-existence of two distinct morphologies: disordered layer of surface reaction and VA-MoS_2. Using the model, we show the underlying principles to achieve control over the structural features and the associated electronic properties. Details of the model are described in the supporting information, and in Fig. S6. In this model the random MoS_2 extends from the surface to a time-dependent depth x_0, and the VA-MoS_2 extends from x_0 to x_1. The model assumes that: (i) Mo is stationary and the reaction is driven by sulfur diffusion only; (ii) sulfur is fully reacted and no inclusions exist in the Mo film; (iii) the consumption of sulfur takes place at the moving boundary between Mo and MoS_2, *i.e.*, at the reaction front.

The set of Eq. (1) present the model for an equilibrium growth at the Mo-MoS_2 interface[38], while the initial and boundary conditions are fit to represent the conditions of the chemical process.

$$\begin{aligned} \frac{\partial C}{\partial t} &= D_{MoS_2}\frac{\partial^2 C}{\partial x^2},\ 0 \le x \le x_0(t) \\ & \qquad\qquad\qquad\qquad 0 < t < \tau \\ \frac{\partial C}{\partial t} + \frac{\partial \eta}{\partial t} &= D_{Mo}\frac{\partial^2 C}{\partial x^2},\ x_0(t) \le x \le \infty \end{aligned} \tag{1}$$

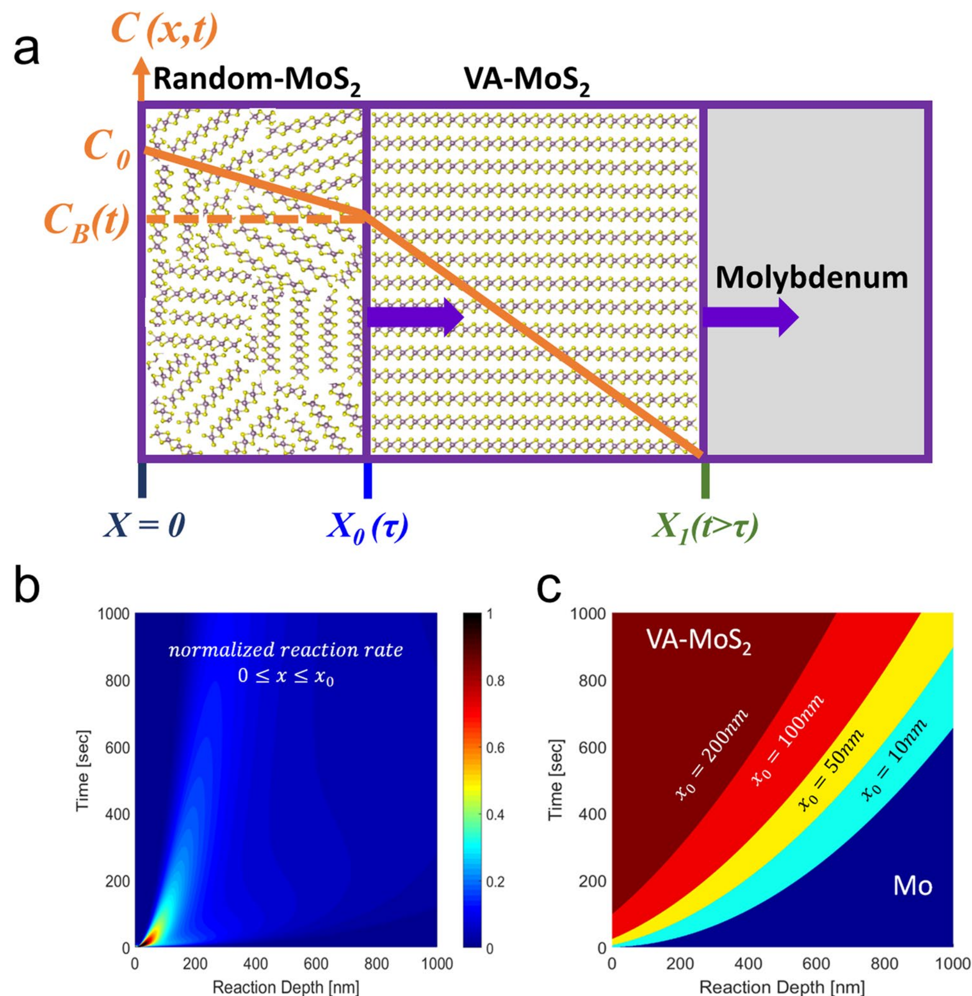

Figure 3. (**a**) Graphical illustration of growth process starting from a surface reaction of depth x_0 and reaction time τ, followed by a diffusion-limited growth of VA-MoS_2. (**b**) The solution to the propagation velocity of $x_0(t)$ with a scaled amplitude showing its rapid decay and (**c**) the resulting VA-MoS_2 growth with several values for x_0.

Here, C is the sulfur concentration and D_{Mo} *and* D_{MoS_2} are the diffusion coefficients of sulfur in Mo and in MoS_2, respectively; η is the concentration of Mo consumed at the interface which is linearly related to C by the constant R by $\eta(x,\ t) = RC(x,\ t)$. $x_0(t)$ is the position of the reaction front, representing the moving boundary of the Mo-MoS_2 interface. The reaction obeys the following conditions: initially, the sample comprises Mo only $[x_0(t \le 0) = 0]$. The self-limited (see SI for details) reaction time for the growth of random MoS_2 is τ: $[x_0(t \ge \tau) = x_0(\tau)]$. The random layer grown within time τ forms a diffusion barrier and the reaction rate, dx_0/dt- decays after τ (see Fig. 3b), where the reaction becomes diffusion-limited. From this point, the growth front advances through vertical seeds and is dominated by the higher diffusion kinetics of sulfur along the Van- der Waals gap that defines the fast axis within MoS_2 with a diffusion coefficient $D_\perp$ for sulfur. Therefore, the reaction continues along a new Mo/VA-MoS_2 interface that we label as $x_1(t > \tau)$. Figure 3a schematically displays our model at which a surface reaction advances from the molybdenum surface into its depth, up to a distance $x_0(\tau)$- followed by a diffusion-limited growth along the fast axis of MoS_2 that obeys Eq. (1), with a time-dependent boundary condition $C_B(t) = C(x_0, t > \tau)$:

$$C_B(x_0,\ t) = C_0 erfc\left(\frac{x_0}{2\sqrt{D_\perp t}}\right),\ t > \tau \tag{2}$$

Figure 3b shows the scaled reaction front velocity, dx_0/dt, as obtained from the analytical solution (see SI for the full solution), showing that the surface reaction dominates the initial stages of the growth. Figure 3c provides the solution $x_1(t)$ - the thickness of VA-MoS_2 with several values of the disoriented film thickness - $x_0(\tau)$, demonstrating the role of this diffusion barrier layer and its impact on growth kinetics, being a barrier for sulfur diffusion. The diffusion coefficients and the parameter R can be calculated from *ab-initio* and molecular dynamics of Mo and sulfur[32,34,36,37].

In some cases, the existence of a randomly oriented layer may be desired and can serve as a diffusion barrier in several processes, such as intercalation, that are widely spread across various applications. In case that a sharp interface is required, this layer can be removed by dry etching.

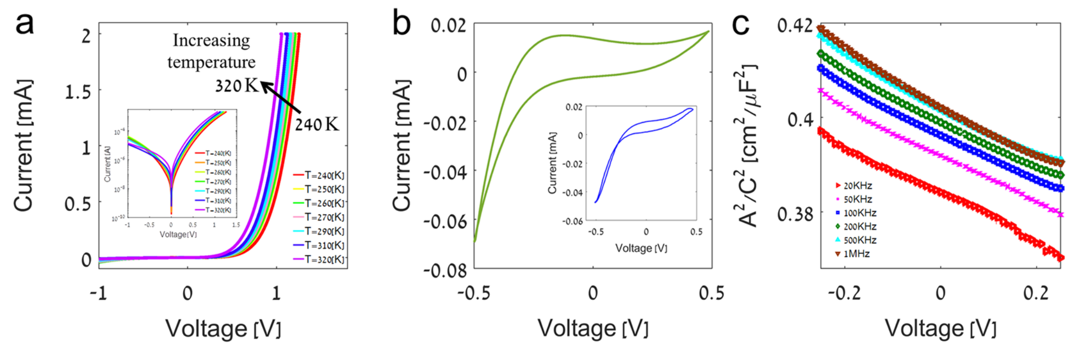

Figure 4. Electrical characterization of Si – VA-MoS_2 heterostructure p-n diode. (**a**) Temperature dependent I-V curves (inset: logarithmic scale), (**b**) cyclic I-V curve at 10 Hz (inset: 100 kHz), and (**c**) voltage-capacitance curves.

It is well known that defects in MoS_2 films are the main source for charge carriers[39–42], which raises the question of the quality of devices made with VA-MoS_2. The disordered layer contains unique structural features and their influence on the electronic properties is so far unexplored. To this end, we prepared diodes from VA-MoS_2 grown on p^+-Si (similar to the sample presented in Fig. 2a), and we confirmed that they obey the standard model of diffusive transport (Fig. 4a), $I = I_0(\exp[qV/\eta k_B T] - 1)$. On these well-behaved diodes we could measure the electrical characteristic of the carriers and the impact of charge traps. Figure 4b shows a sizable hysteresis under cyclic bias applied on the diodes, corresponding to charge trapping at crystalline defects, rendering them polar[43–45]. By analogy with polar ions observed in perovskites[46], we assign this electrical behavior to trap charging and discharging. The quenching of the hysteresis with increased frequency is a result of the trap capacitance and the resulting trapping/detrapping rate. From the capacitance measurements in Fig. 4c, the estimation of the built-in potential is 1.2 eV and the carrier density is ~10^{19} cm^{-3}. The measured built-in potential represents the p-n quasi-Fermi level difference and the band misalignment across the junction that can be roughly estimated to ~100 meV in this case of highly doped, sharp junction. We assume that the measured carrier density is comparable with the density of traps ($N_t \approx N_D$) and that the vast majority of carriers in VA-MoS_2 originate from shallow traps[47,48].

To conclude, we analyzed the growth of MoS_2 by sulfurization of metallic Mo films from several perspectives. We applied a high-temperature, low pressure growth on thin film Mo resulting in a gradual transition from disordered crystalline MoS_2 to a vertically oriented morphology. By applying a theoretical diffusion-reaction model to the growth, we provided a plausible growth mechanism that explains the experimental observations. Our model is general and applicable to a large variety of layered materials. If provided with diffusion parameters retrieved from experiments or *ab-initio* calculations, it will provide a predictive, quantitative tool to characterize the growth process. Regarding the electronic properties of samples containing a disordered layer, we found that the band misalignment between Si and VA-MoS_2 can be estimated to ~100 meV and that structural defects result in trap states that can be observed in cyclic I-V measurements. Details of the trap energy and density are a subject for future work. Yet without loss of generality, we conclude that rapid reactions result in higher defect density and that the surface reaction taking place at the beginning of the process is the source for the majority of defects. These conclusions may have critical implications to the performance of VA-MoS_2 in several fields including catalysis, lithium ion storage and solar energy harvesting and optoelectronics devices.

Methods

Sample preparation.

Si wafer preparation. Photolithography was applied to a sample of 90 nm SiO_2/Si P-type wafer to create an array of 324 circles of 40 µm diameter each. The oxide layer in the circles was then selectively etched by reactive-ion etching, followed by evaporation and lift-off of ~30 nm Molybdenum, after which the CVD process was applied. Metal contacts were finally deposited by e-beam lithography and evaporation.

CVD process.

Si wafer. Samples were annealed under 160 sccm N_2 flow at 200 °C for 1 h. Sulfur powder was placed upstream at low temperature zone of ~150 °C. The quartz furnace was heated (20 °C/min and 5 °C/min, for the fast/slow temperature ramping samples, respectively) to 800 °C under 30 sccm nitrogen flow and were held at this set-point for 2 h. Then the temperature was reduced to 600 °C, the sulfur was solidified and afterwards the temperature was reduced (7 °C/min until 400 °C and afterward 2 °C/min till reaches to room temperature).

Mo foil. The sample was annealed under 160 sccm N_2 flow at 200 °C for 1 h. Sulfur powder was placed upstream at low temperature zone of ~150 °C until liquefied. The quartz furnace was heated to 500 °C (20 °C/min) under 100 sccm nitrogen flow and was held at this set point for 30 min. Subsequently the quartz furnace was heated to 600 °C (20 °C/min) under a nitrogen flow of 100 sccm and it was held at this set point for a period of 30 min. An additional heating step was added while the temperature rose to 750 °C (20 °C/min) under a 30 sccm nitrogen flow. This state was maintained for a period of 24 h. In the last thermal cycling step the temperature was reduced to 600 °C, the sulfur was solidified and the temperature was further reduced to 400 °C (5 °C/min) and then brought down to room temperature (2 °C/min). Further details and a graphical representation of the temperature cycle are presented in the supporting information.

TEM. TEM lamella of the CVD-grown VA-MoS_2 devices were prepared using a FEI Helios 600 Focused Ion Beam (FIB) microscope. Pt was deposited during the FIB process for the purpose of material protection. TEM micrographs of the cross-sectional device samples were collected on a JEOL JEM-2100 high resolution transmission electron microscope operated at 200 kV.

Raman Spectroscopy. Raman spectra were taken by a Horiba Scientific Labram HR Evolution using a 532 nm laser. The exciting laser propagated parallel to the crystal c-axis with a linear polarization.

Electrical measurements. Samples were wire bonded to ceramic leadless chip carrier, and then were measured in a cryostat vacuum chamber (Montana instruments) with a Keysight B2912A and B1500A instruments.

References

1. Lee, Y. H. *et al*. Synthesis of large-area MoS_2 atomic layers with chemical vapor deposition. *Adv. Mater.* **24**, 2320–2325 (2012).
2. Wang, X., Feng, H., Wu, Y. & Jiao, L. Controlled synthesis of highly crystalline MoS_2 flakes by chemical vapor deposition. *J. Am. Chem. Soc* **135**, 5304–5307 (2013).
3. Amani, M. *et al*. Electrical performance of monolayer MoS_2 field-effect transistors prepared by chemical vapor deposition. *Appl. Phys. Lett.* **102**, 193107 (2013).
4. Radisavljevic, B., Radenovic, A., Brivio, J., Giacometti, I. V. & Kis, A. Single-layer MoS_2 transistors. *Nature nanotechnology* **6**, 147–150 (2011).
5. Jariwala, D., Sangwan, V. K., Lauhon, L. J., Marks, T. J. & Hersam, M. C. Emerging device applications for semiconducting two-dimensional transition metal dichalcogenides. *ACS nano* **8**, 1102–1120 (2014).
6. Radisavljevic, B., Whitwick, M. B. & Kis, A. Integrated circuits and logic operations based on single-layer MoS_2. *ACS nano* **5**, 9934–9938 (2011).
7. Wang, H. *et al*. Integrated circuits based on bilayer MoS_2 transistors. *Nano Lett.* **12**, 4674–4680 (2012).
8. Xu, X., Yao, W., Xiao, D. & Heinz, T. F. Spin and pseudospins in layered transition metal dichalcogenides. *Nature Physics* **10**, 343–350 (2014).
9. Mak, K. F., McGill, K. L., Park, J. & McEuen, P. L. The valley Hall effect in MoS_2 transistors. *Science* **344**, 1489–1492 (2014).
10. Wu, S. *et al*. Vapor–solid growth of high optical quality MoS_2 monolayers with near-unity valley polarization. *Acs Nano* **7**, 2768–2772 (2013).
11. Tongay, S. *et al*. Tuning interlayer coupling in large-area heterostructures with CVD-grown MoS_2 and WS_2 monolayers. *Nano Lett.* **14**, 3185–3190 (2014).
12. Gong, Y. *et al*. Vertical and in-plane heterostructures from WS_2/MoS_2 monolayers. *Nature materials* **13**, 1135–1142 (2014).
13. Hong, X. *et al*. Ultrafast charge transfer in atomically thin MoS_2/WS_2 heterostructures. *Nature nanotechnology* **9**, 682–686 (2014).
14. Roy, T. *et al*. Dual-gated MoS_2/WSe2 van der Waals tunnel diodes and transistors. *Acs Nano* **9**, 2071–2079 (2015).
15. Li, M.-Y. *et al*. Epitaxial growth of a monolayer WSe2-MoS_2 lateral pn junction with an atomically sharp interface. *Science* **349**, 524–528 (2015).
16. Yu, J. H. *et al*. Vertical heterostructure of two-dimensional MoS_2 and WSe2 with vertically aligned layers. *Nano Lett.* **15**, 1031–1035 (2015).
17. Wang, H. *et al*. Electrochemical tuning of vertically aligned MoS_2 nanofilms and its application in improving hydrogen evolution reaction. *Proceedings of the National Academy of Sciences* **110**, 19701–19706 (2013).
18. Jung, Y. *et al*. Metal seed layer thickness-induced transition from vertical to horizontal growth of MoS_2 and WS_2. *Nano Lett.* **14**, 6842–6849 (2014).
19. Zhang, X. *et al*. Direct synthesis of large-scale hierarchical MoS_2 films nanostructured with orthogonally oriented vertically and horizontally aligned layers. *Nanoscale* **8**, 431–439 (2015).
20. Qiao, S. *et al*. Large lateral photovoltage observed in MoS_2 thickness-modulated ITO/MoS_2/p-Si heterojunctions. *ACS Applied Materials & Interfaces* (2017).
21. Mao, J. *et al*. Ultrafast, Broadband Photodetector Based on MoSe2/Silicon Heterojunction with Vertically Standing Layered Structure Using Graphene as Transparent Electrode. *Advanced Science* **3**, 1600018 (2016).
22. Dhyani, V. & Das, S. High-Speed Scalable Silicon-MoS_2 PN Heterojunction Photodetectors. *Scientific Reports* **7**, 44243 (2017).
23. Zhang, Y. *et al*. *In Situ* Fabrication of Vertical Multilayered MoS_2/Si Homotype Heterojunction for High-Speed Visible–Near-Infrared Photodetectors. *Small* **12**, 1062–1071 (2016).
24. Cheng, R. *et al*. Electroluminescence and photocurrent generation from atomically sharp WSe2/MoS_2 heterojunction p–n diodes. *Nano Lett.* **14**, 5590–5597 (2014).
25. Gao, J. *et al*. Vertically oriented arrays of ReS2 nanosheets for electrochemical energy storage and electrocatalysis. *Nano Lett.* **16**, 3780–3787 (2016).
26. Chao, D. *et al*. Pseudocapacitive Na-ion storage boosts high rate and areal capacity of self-branched 2D layered metal chalcogenide nanoarrays. *ACS nano* **10**, 10211–10219 (2016).
27. Wang, L. *et al*. MoS_2/Si Heterojunction with Vertically Standing Layered Structure for Ultrafast, High-Detectivity, Self-Driven Visible–Near Infrared Photodetectors. *Adv. Funct. Mater.* **25**, 2910–2919 (2015).
28. Bichsel, R. & Levy, F. Morphological and compositional properties of MoSe2 films prepared by r.f. magnetron sputtering. *Thin Solid Films* **116**, 367–372 (1984).
29. Bertrand, P. A. Orientation of rf-sputter-deposited MoS_2 films. *Journal of Materials Research* **4**, 180–184 (1989).
30. Shokhen, V. *et al*. On the impact of Vertical Alignment of MoS_2 for Efficient Lithium Storage. *Scientific Reports* **7** (2017).
31. Zhan, Y., Liu, Z., Najmaei, S., Ajayan, P. M. & Lou, J. Large-area vapor-phase growth and characterization of MoS_2 atomic layers on a SiO2 substrate. *Small* **8**, 966–971 (2012).
32. Shang, S.-L. *et al*. Lateral versus vertical growth of two-dimensional layered transition-metal dichalcogenides: Thermodynamic insight into MoS_2. *Nano Lett.* **16**, 5742–5750 (2016).
33. Kong, D. *et al*. Synthesis of MoS_2 and MoSe2 films with vertically aligned layers. *Nano Lett.* **13**, 1341–1347 (2013).
34. Rajan, A. G., Warner, J. H., Blankschtein, D. & Strano, M. S. Generalized mechanistic model for the chemical vapor deposition of 2D transition metal dichalcogenide monolayers. *ACS Nano* **10**(4), 4330–4344 (2016).
35. Zhu, D. *et al*. Capture the growth kinetics of CVD growth of two-dimensional MoS_2. *npj 2D Materials and Applications* **1**, 8 (2017).
36. Nie, Y. *et al*. A kinetic Monte Carlo simulation method of van der Waals epitaxy for atomistic nucleation-growth processes of transition metal dichalcogenides. *Scientific Reports* **7**, 2977 (2017).
37. Nie, Y. *et al*. First principles kinetic Monte Carlo study on the growth patterns of WSe2 monolayer. *2D Materials* **3**, 025029 (2016).
38. Crank, J. *The mathematics of diffusion*. (Oxford university press, 1979).
39. Li, H. *et al*. Kinetic study of hydrogen evolution reaction over strained MoS_2 with sulfur vacancies using scanning electrochemical microscopy. *J. Am. Chem. Soc.* **138**, 5123–5129 (2016).

40. Sim, D. M. *et al.* Controlled doping of vacancy-containing few-layer MoS_2 via highly stable thiol-based molecular chemisorption. *ACS nano* **9**, 12115–12123 (2015).
41. Kim, S. *et al.* Effects of plasma treatment on surface properties of ultrathin layered MoS_2. *2D Materials* **3**, 035002 (2016).
42. Zhou, W. *et al.* Intrinsic structural defects in monolayer molybdenum disulfide. *Nano Lett.* **13**, 2615–2622 (2013).
43. Lee, E. G., Wouters, D. J., Willems, G. & Maes, H. E. Voltage shift and deformation in the hysteresis loop of Pb (Zr, Ti) O3 thin film by defects. *Appl. Phys. Lett.* **69**, 1223–1225 (1996).
44. Prosandeyev, S. *et al.* Study of intrinsic point defects in oxides of the perovskite family: I. Theory. *J. Phys.: Condens. Matter* **8**, 6705 (1996).
45. Park, C. & Chadi, D. Microscopic study of oxygen-vacancy defects in ferroelectric perovskites. *Physical Review B* **57**, R13961 (1998).
46. Meloni, S. *et al.* Ionic polarization-induced current–voltage hysteresis in CH3NH3PbX3 perovskite solar cells. *Nature communications* **7**, 10334 (2016).
47. Lu, C.-P., Li, G., Mao, J., Wang, L.-M. & Andrei, E. Y. Bandgap, mid-gap states, and gating effects in MoS_2. *Nano letters* **14**, 4628–4633 (2014).
48. Radisavljevic, B. & Kis, A. Mobility engineering and a metal–insulator transition in monolayer MoS_2. *Nature Materials* **12**, 815 (2013).

Acknowledgements

DN would like to thank the Israeli Science Foundation for funding of this work with grant #1055/15. The authors would like to thank Yafit Fleger for preparing TEM sample using focused ion beam, Ilana Perelshtein for assistance with TEM imaging.

Author Contributions

C.S. performed CVD growth; C.S., H.A. and M.O. fabricated the devices; C.S., S.G., M.K. and O.S. performed electrical measurements; D.N., S.G. and C.S. analyzed the results; M.B.S. and O.E.M. conducted TEM measurements, M.B.S. and L.H. analyzed TEM images; all authors read and agreed with the manuscript.

Additional Information

Supplementary information accompanies this paper at https://doi.org/10.1038/s41598-018-34222-z.

Competing Interests: The authors declare no competing interests.

Publisher's note: Springer Nature remains neutral with regard to jurisdictional claims in published maps and institutional affiliations.

Open Access This article is licensed under a Creative Commons Attribution 4.0 International License, which permits use, sharing, adaptation, distribution and reproduction in any medium or format, as long as you give appropriate credit to the original author(s) and the source, provide a link to the Creative Commons license, and indicate if changes were made. The images or other third party material in this article are included in the article's Creative Commons license, unless indicated otherwise in a credit line to the material. If material is not included in the article's Creative Commons license and your intended use is not permitted by statutory regulation or exceeds the permitted use, you will need to obtain permission directly from the copyright holder. To view a copy of this license, visit http://creativecommons.org/licenses/by/4.0/.

© The Author(s) 2018